



Article

PrecipGradeNet: A New Paradigm and Model for Precipitation Retrieval with Grading of Precipitation Intensity

Danfeng Zhang ^{1,†}, Yuqing He ^{1,†} , Xiaoqing Li ², Lu Zhang ² and Na Xu ^{2,*}¹ School of Optics and Photonics, Beijing Institute of Technology, Beijing 100081, China² Innovation Center for Fengyun Meteorological Satellite, National Satellite Meteorological Center, China Meteorological Administration, Beijing 100081, China

* Correspondence: xuna@cma.gov.cn

† These authors contributed equally to this work.

Abstract: Near-real-time precipitation retrieval plays an important role in the study of the evolutionary process of precipitation and the prevention of disasters caused by heavy precipitation. Compared with ground-based precipitation observations, the infrared precipitation estimations from geostationary satellites have great advantages in terms of geographical coverage and temporal resolution. However, precipitation retrieved from multispectral infrared data still faces challenges in terms of accuracy, especially in extreme cases. In this paper, we propose a new paradigm for satellite multispectral infrared data retrieval of precipitation and construct a new model called PrecipGradeNet. This model uses FY-4A L1 FDI data as the input, IMERG precipitation data as the training target, and improves the precipitation retrieval accuracy by grading the precipitation intensity through Res-UNet, a semantic segmentation network. To evaluate the precipitation retrieval of the model, we compare the retrieval results with the FY-4A L2 QPE operational product to the IMERG precipitation. IMERG is considered as the ground truth. We evaluate the precipitation retrieval from the precipitation fall area identification, the precipitation intensity interval discrimination, and the precipitation quantification. Experimental results show that PrecipGradeNet has better overall performance compared with the FY-4A QPE product in precipitation fall area identification with POD increased by 48% and CSI and HSS improved by 21% and 14%. PrecipGradeNet also has better performance in light precipitation with POD increased by 114% and CSI and HSS improved by 64% and 52%, and better overall precipitation quantification, with RMSE and CC improved by 16% and 15%. In addition, PrecipGradeNet avoids the overall bias in the low and extreme high precipitation cases. Therefore, the new paradigm proposed in this paper has the potential to improve the retrieval accuracy of satellite precipitation estimation products. This study suggests that the application of semantic segmentation methods may provide a new path to correct the intensity bias of the satellite-based precipitation products.



Citation: Zhang, D.; He, Y.; Li, X.; Zhang, L.; Xu, N. PrecipGradeNet: A New Paradigm and Model for Precipitation Retrieval with Grading of Precipitation Intensity. *Remote Sens.* **2023**, *15*, 227. <https://doi.org/10.3390/rs15010227>

Academic Editors: Jianguang Wen, Shaomin Liu and Qinhuo Liu

Received: 8 November 2022

Revised: 25 December 2022

Accepted: 25 December 2022

Published: 31 December 2022



Copyright: © 2022 by the authors. Licensee MDPI, Basel, Switzerland. This article is an open access article distributed under the terms and conditions of the Creative Commons Attribution (CC BY) license (<https://creativecommons.org/licenses/by/4.0/>).

Keywords: geostationary satellite; FY-4A satellite; multispectral infrared imagery; quantitative precipitation estimation; semantic segmentation; Res-UNet

1. Introduction

The Asian monsoon is one of the most important components of the global climate system [1]. It plays an important role in the climate system, coupling energy and water cycles [2,3]. Precipitation data derived from ground-based observations were widely used in early studies of interdecadal, interannual, and daily variability of precipitation in the Asian monsoon zone [3–6]. Although ground-based rain gauges and ground-based weather radar are capable of measuring precipitation with high temporal and spatial resolution [5], they have a major drawback for spatial coverage that is unable to cover large lakes, oceans, and mountainous areas, and also less populated areas such as Africa, Antarctica, etc. Moreover, various observation errors can also have a large impact on data applications. Evaporation, splash and wind effects can lead to less precipitation observed

by rain gauges when conventional rain gauges collect precipitation. Meanwhile, radar must cope with beam blockage in mountainous areas, anomalous propagation errors, and imprecise backscattering in relation to rainfall rates [7,8]. The observation range of satellite PMW (passive microwave) data is not affected by ground conditions, which makes satellites an important source of supplementary data for the observation of precipitation and largely fills the problem of insufficient ground-based observation coverage [7–9].

However, due to the wavelength limitations of microwaves, PMW sensors are currently only carried on polar-orbiting meteorological satellites. This results in the spatial and temporal sampling limitations of PMW precipitation products, and the same sensor has only two observations per day for the same area at low and mid latitudes [10]. Optical instruments of the geosynchronous orbit satellites can achieve continuous observation of the same location and have higher spatial resolution than microwave observation [11]. Furthermore, the quantitative precipitation products retrieved from them also have a high temporal and spatial resolution. However, the infrared channel can only indirectly derive the ground precipitation intensity from the cloud-top brightness temperature observations, so the accuracy of the precipitation retrieval is limited [12–14]. Compared to infrared sensors, PMW sensors can detect the underlying surface of precipitation more effectively through clouds [7]. Several techniques have been developed to combine the microwave and infrared information to estimate the precipitation, taking advantage of the accuracy of microwave estimation and the low error of infrared sampling [12,15].

Traditional methods of combining microwave and infrared data generally include morphing PMW precipitation data using the motion trends of infrared images [10] and using thresholds to classify different situations of microwaves calibrating the infrared precipitation [14]. However, the use of deformation suffers from a problematic response speed for rapid changes in precipitation [16], and the traditional threshold method for strong precipitation retrieval suffers from the problem of conservative estimation due to the high tendency of target precipitation rate towards light precipitation [14]. Due to the excellent fitting of various types of nonlinear relations by machine learning (ML) methods, ML methods such as support vector machines [17], random forests [15,18,19], and deep learning (DL) [20–24] have been successfully applied in precipitation-retrieval studies.

It is noted in this article that previous studies of precipitation retrieval methods have been based almost entirely on the paradigm of first determining precipitation areas and then regressing the areas determined to contain precipitation. However, due to the high tendency of precipitation samples towards light precipitation and the differences in the infrared (IR) characteristics of different precipitation intensity and precipitation types, it is often difficult to guarantee the accuracy of retrieval methods for both light and heavy precipitation, grouping all precipitation into one category. There are frequent cases of overall underestimation of precipitation under very heavy precipitation [10,19,25] or overflow of discrimination in areas of heavy precipitation [14,15] as well as misdetection [26] or overall overestimation [27] of light precipitation.

To improve the deficiency of retrieval accuracy under extreme precipitation conditions, especially under extreme heavy precipitation due to the infrared retrieval precipitation method that groups all precipitation into one category, we constructed a new research method and a new model called PrecipGradeNet. First, the precipitation intensity intervals were graded using infrared features obtained from FY-4A L1 FDI and PMW precipitation data, and then the precipitation was regressed by combining the infrared features with the precipitation intensity intervals. This method improves the retrieval capability to deal with extreme cases by classifying precipitation of different intensities into different classes for separately retrieving. Using this approach, PrecipGradeNet can reduce the influence of the accuracy of precipitation retrieval on the difference of precipitation characteristics of different intensities and the uneven number of precipitation image elements of different intensities.

This paper is organized as follows. Section 2 describes the data used in PrecipGradeNet training, including infrared and microwave data. We describe the scheme design of the

retrieval method and the detailed steps of the experiments in Section 3 and then describe the process of model training and the validation results in Section 4. Section 5 gives the evaluation of the retrieval of PrecipGradeNet for the applied dataset and the performance of the application in two typical individual cases. In Section 6, we give conclusions on the experimental and applied results and discuss the possibilities of future development of the method.

2. Data

2.1. Interesting Geographical Regions

The geographic area studied in this paper was 20°N–33°N, 100°E–125°E, as Figure 1 shows, which covers the tropical monsoon and subtropical monsoon regions of southeast China and the offshore regions of China, generating large amounts of precipitation in summer, which has a large impact on local life.

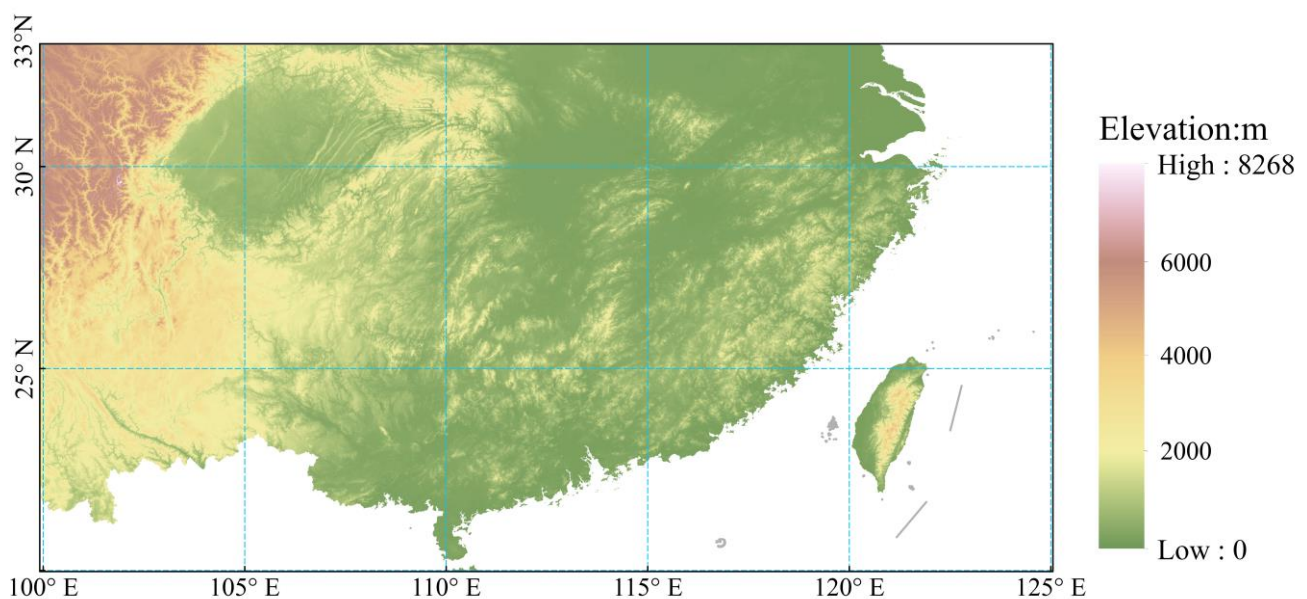


Figure 1. The elevation map of the geographic area studied in this paper.

2.2. FY-4 L1 FDI Data

The Fengyun-4 series of meteorological satellites is the second generation of China's geostationary meteorological satellites, and FY-4A is the first satellite in the series, launched in 2016 and located over the equator at 104.7°E. One of the main payloads carried by the satellite is the multi-channel scanning imaging radiometer AGRI (Advanced Geosynchronous Radiation Imager), which has more bands and higher imaging quality than the visible infrared scanning radiometer (VISSR) carried by the Fengyun-2 series satellites [28]. Table 1 lists the wavelengths, resolutions, and main observation targets of AGRI's different channels. AGRI makes a complete observation of the full disk in 15 min [29]. Channels 9–13 of AGRI contain water vapor and cloud-top brightness temperature information, which have a strong correlation with precipitation, and previous studies have also shown that the cloud-top brightness temperature of convective precipitation clouds is generally low [11,30]. Therefore, we used the infrared information of channels 9–13 to construct the relationship between infrared data and precipitation intensity for precipitation retrieval.

Table 1. FY-4A AGRI spectral band and main detection objects.

Channel Number	Channel Type	Band Wavelength Range/ μm	Spatial Resolution/km	Detection Objects	Channels Used in This Article
1	Visible & Near-Infrared	0.45–0.49	1	Small particle aerosol	
2		0.55–0.75	0.5–1	Fog, Cloud	
3		0.75–0.90	1	Vegetation	
4	Short-Wave Infrared	1.36–1.39	2	Cirrus	
5		1.58–1.64	2	Cloud, Snow	
6		2.1–2.35	2–4	Cirrus, Aerosol	
7	Mid-Wave Infrared	3.5–4.0 (High)	2	Fire	
8		3.5–4.0 (Low)	4	Land surface	
9	Water Vapor	5.8–6.7	4	High Water Vapor	✓
10		6.9–7.3	4	Middle Water Vapor	✓
11	Long-Wave Infrared	8.0–9.0	4	Total Water Vapor	✓
12		10.3–11.3	4	Clouds, surface temperature	✓
13		11.5–12.5	4	Clouds, total water vapor	✓
14		13.2–13.8	4	Cloud, water vapor	

2.3. Precipitation Products

The target precipitation data used in this study was sourced from the Integrated Multi-satellite Retrievals for Global Precipitation Measurement (IMERG) product, a Level 3 precipitation product of the NASA/JAXA GPM (Global Precipitation Measurement) [8]. It includes mainly HQprecipitation, which merges passive microwave data, IRprecipitation, which combines IR and microwave, and precipitationCal, which uses ground-based rain-gauge calibrations. In this study, we used HQprecipitation, which contains only high-quality passive microwave data in IMERG, in order to ensure the accuracy of precipitation data. IMERG precipitation data is a merged product based on PMW data from multiple satellites, which obtains a higher temporal resolution than individual satellites by merging PMW images from different satellites. As of 2021, the product has used PMW data from 11 satellites [7,8]. Previous studies have shown that IMERG products perform better than other satellite precipitation datasets such as TRMM Multi-satellite Precipitation Analysis (TMPA) 3B42/3B42RT [31]. IMERG provides three versions of precipitation product, named Early, Late, and Final. The Early product is generated in real time using microwave data merging and has a delay of about 4 h in release from the real-time data, the Late product has a larger delay of about 14 h due to the inclusion of both forward and backward estimation, and the Final product is calibrated with the rain gauge and has a delay of several months. The final product has the highest accuracy, but there is a large time delay. The Late product is initially corrected, but is less effective than the Early product in some cases of sparse precipitation [32]. HQprecipitation data in the Early product has the lowest time delay and certain accuracy in precipitation retrieval compared to IR precipitation data, which can meet the real-time and accuracy requirements of the application. Therefore, this paper adopts the Early product as the target for training and treats it as the true value of precipitation on the ground. The IMERG product has a temporal resolution of 30 min, the observation time of each image element is accurate to the minute, and the spatial resolution is 0.1° , distributed on an equal latitude and longitude grid.

The FY-4A infrared precipitation estimation operational product (QPE) is chosen to compare with PrecipGradeNet to see if PrecipGradeNet has superiority over the operational products. QPE is a secondary operational product of the FY-4A satellite, obtained by retrieving brightness temperature data observed by the infrared channel of AGRI using a probability density matching method [33]. The 15-min FY-4A L2 QPE product has the same

temporal and spatial resolution as the FY-4A L1 FDI [34]. Since the FY-4A L2 QPE product is also obtained from the FY-4A L1 FDI IR data, it can be used as a suitable comparison product for PrecipGradeNet.

3. Methodology

3.1. Method Procedure

Figure 2 shows the flowchart of the method. It consists of two parts. The left part describes the training process of the model, and the right one describes the method of using the model in the validation and application processes. In the training session, this paper first establishes the consistency between the infrared observation data and IMERG products on spatial and temporal scales, and then applies these data to the semantic segmentation network and regression network training, respectively. In the testing and application sessions, the predicted precipitation levels and other data are outputted from the segmentation network and fed into the regression network together with the IR data to obtain the predicted precipitation results.

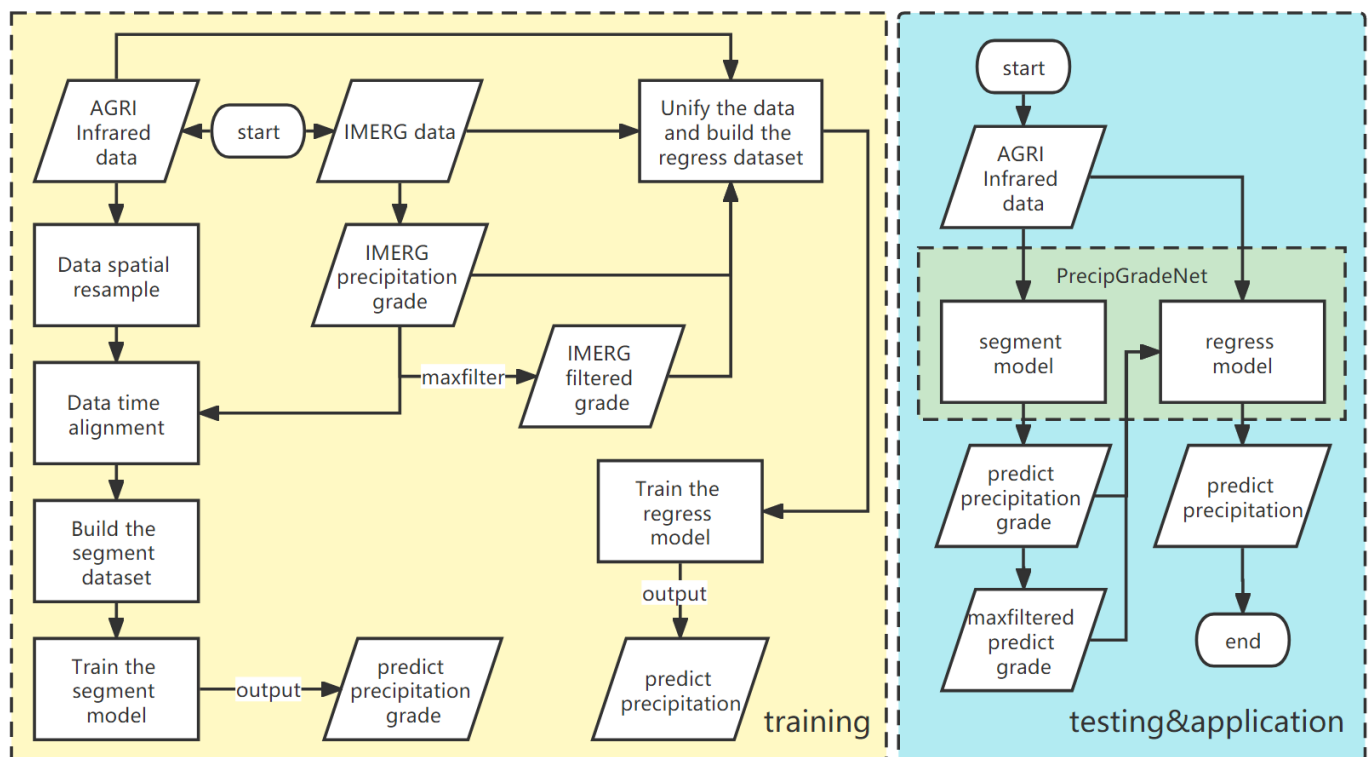


Figure 2. Flow chart of the method.

3.2. Method Design

Different precipitation types exhibit large differences in infrared brightness temperature characteristics. For example, convective precipitation has more ice particles in the upper layer, and the observed cloud-top brightness temperature is obviously low. While the stratiform precipitation system has a weaker vertical development, it is difficult to estimate the land surface precipitation intensity by infrared cloud-top brightness temperature. In addition, there are differences in the patterns of different types of precipitation, with convective precipitation having high precipitation intensity and covering a small area, and stratiform precipitation having low precipitation intensity and covering a large area [35]. The general precipitation intensity interval classification standard [36] is shown in Table 2, and the proportional distribution of different precipitation intensity intervals is shown in Table 3 (This proportion is taken from IMERG precipitation data located in the range of 20°N–33°N, 100°E–125°E from April 2021–July 2021). As seen in Table 3, for a satellite ob-

servation image, precipitation elements account for only a small fraction of the images, and most of the image elements have no precipitation, while light precipitation accounts for the largest part of the image elements with precipitation, and heavy precipitation accounts for only a very small part. Kuligowski et al. demonstrated that the results of direct regression using IR brightness temperature strongly tended to light precipitation, because the target precipitation distribution highly tended to have lower precipitation rates [12]. To solve this problem, some studies have used datasets with a higher percentage of heavy precipitation for training, but the problem of low retrieved precipitation rates still exists [26]. In addition to the imbalance between the amount of light and heavy precipitation, there is also a strong non-linear relationship between IR characteristics and precipitation intensity [37]. In order to solve the problem that light precipitation image elements and heavy precipitation image elements affect each other in the precipitation retrieval process, we segmented the precipitation grades of different intensities to allow PrecipGradeNet to process different precipitation classes of different intensities separately.

Table 2. Precipitation intensity intervals in common use.

Light Rain	Moderate Rain	Heavy Rain
0–2.5 mm/h	2.5–8 mm/h	>8 mm/h

Table 3. Percentage of different precipitation intervals (this proportion is taken from IMERG precipitation data located in the range of 20°N–33°N, 100°E–125°E from April 2021–July 2021).

No Precipitation	Light Rain	Moderate Rain	Heavy Rain
81.39%	15.97%	2.10%	0.54%

To segment the different intensity precipitation grades, we use a method called semantic segmentation. Semantic segmentation is a DL algorithm capable of separating different components in an image, and it is suitable to segment precipitation intensity grades. Through adding weights to different classes in the loss function, it can effectively deal with the extreme imbalance in the number of samples of different precipitation grades.

After segmenting the different precipitation intensity grades, the quantitative retrieval of precipitation data is obtained by regressing the precipitation rates based on the segmented precipitation intensity grades and maximum-filtered (maxfiltered) grades combined with their infrared features.

In summary, PrecipGradeNet consists of two networks with different functions, as shown in Figure 3. The first is a semantic segmentation network that segments the features of infrared images into different precipitation intensity grades. The second is a regression network that combines the precipitation intensity grade and other features for quantitative regression of precipitation rates.

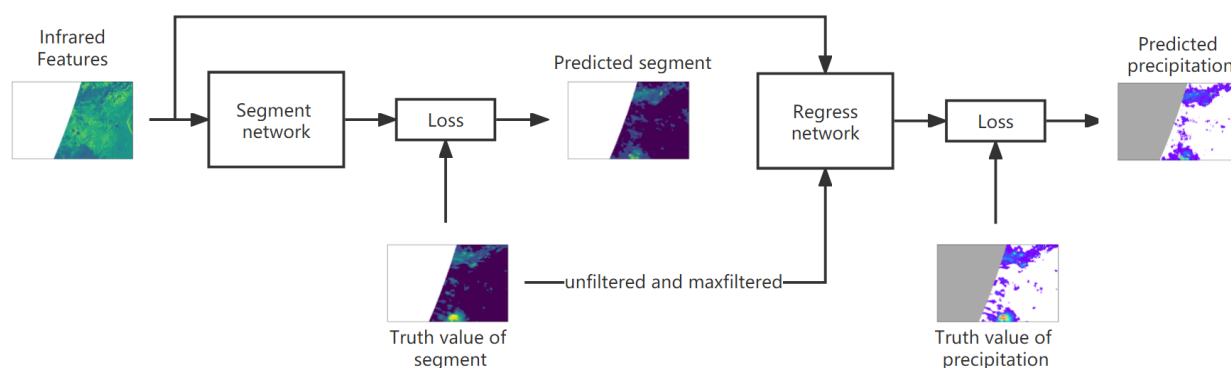


Figure 3. Flow chart of PrecipGradeNet training process.

3.3. PrecipGradeNet Network Structure

PrecipGradeNet consists of two DL networks with UNet-like structure named Res-UNet. UNet is a DL network based on the encoder–decoder structure, which is widely used in remote-sensing image processing because of its excellent performance in image segmentation and extraction of image information [21,24]. Res-UNet is an improved method of UNet, changing the encoder and decoder of UNet from a convolution layer-pooling layer structure to residual block (Resblock) in Resnet. Studies have shown that Res-UNet has better performance and higher accuracy for segmentation of tiny and indistinct features than traditional UNet [38] and is more suitable for the sparse distribution patterns of precipitation.

As a preliminary experiment, due to the indirect relationship between IR brightness temperature and precipitation, there is a large amount of uncertainty in the infrared characteristics of precipitation, and there are limitations in the relationship between IR brightness temperature and quantitative precipitation established directly using machine learning methods. For this reason, Res-UNet does not fit the QPE data effectively by IR brightness temperature data directly, but Res-UNet can isolate different precipitation intensity intervals, which further illustrates the feasibility and necessity of the two-step approach.

As the results of tests on infrared features in the GOES-R ABI precipitation retrieval experiment by Robert, J. et al. [14] show, the brightness temperature difference between IR channels is more significantly related to precipitation intensity than the brightness temperature observations. Therefore, this paper uses a linear combination of eight different channels of IR brightness temperatures [14] as the characteristic quantities of the network and modify the bias constant to avoid negative values in the feature generated by FY-4A L1 FDI, as shown in Table 4. According to previous studies, there is a nonlinear relationship between the precipitation rate and channel 12's brightness temperature. By adjusting the threshold, the brightness temperature value can be made closer to 0 but not negative to make the network more sensitive to the nonlinear relationship between IR characteristics and precipitation intensity. Because precipitation does not always occur at the location of the lowest brightness temperature at the cloud top, we also used the regional brightness temperature minimum in a 5×5 window (5×5 minimum) and its linear combination with the regional brightness temperature mean in a 5×5 window (5×5 average) as features to enhance the precipitation characteristics.

Table 4. Infrared brightness temperature characteristics. The number in subscripts refers to the channel used, T_{\min} refers to the 5×5 minimum of the channel, and T_{avg} refers to the 5×5 average of the channel.

Input Layer ID	Description
1	$T_9 - 174$
2	$0.568 * (T_{\min(12)} - 217) + 25$
3	$T_{\text{avg}(12)} - T_{\min(12)} - (L2 * - 25) + 85$
4	$T_{10} - T_9 + 60$
5	$T_{11} - T_{10} + 60$
6	$T_{12} - T_{10} + 20$
7	$T_{11} - T_{12} + 30$
8	$T_{12} - T_{13} + 20$

*: L2 is the calculation result of layer2.

Table 5 lists the division of precipitation intensity grades by the semantic segmentation network. To improve the precision of the segmentation of the semantic segmentation network, we have refined the precipitation level of the semantic segmentation network to 10 more refined levels. Since the percentage of light precipitation image elements in the observed images is much higher than that of strong precipitation, and the distribution of precipitation intensity is very unbalanced, it is necessary to classify the light precipitation in a more detailed way than heavy precipitation in the semantic segmentation network, so

the intensity interval between precipitation grades for light precipitation is smaller than that for heavy precipitation.

Table 5. Segment network precipitation grade, grade number, and the number of pixels each grade (number of pixels is obtained from IMERG precipitation data from 4 August 2021 to 7 October 2021).

Precipitation Grade Num	0	1	2	3	4	5
Precipitation Range	no data	0 mm/h	0 mm/h–1 mm/h	1 mm/h–2.5 mm/h	2.5 mm/h–5 mm/h	5 mm/h–8 mm/h
Number of Pixels		2,717,195	444,400	110,316	55,350	22,021
Precipitation Grade num	6	7	8	9	10	
Precipitation Range	8 mm/h–12 mm/h	12 mm/h–15 mm/h	15 mm/h–20 mm/h	20 mm/h–30 mm/h	30 mm/h+	
Number of Pixels	11,561	4023	2850	1757	1470	

Figure 4 shows the structure of the Res-UNet as semantic segmentation network in PrecipGradeNet and the structure of Resblock. The semantic segmentation network is Res-UNet, an encoder–decoder structured network with cross-layer connections, which can acquire precipitation features from infrared data at different scales. To extract smaller precipitation features more accurately, the up-sampling (blue arrow) and down-sampling (green arrow) of the feature map in Figure 4a are performed using the Resblock, which consists of two sets of convolutional layers with shortcut stacked together, as shown in Figure 4b. Figure 4a shows the schematic diagram of Res-Unet: the left part of the figure is the encoder, while the right part is the decoder. The blue box indicates the feature channels, the red box indicates the shortcut layer, the yellow box indicates the prediction result, the width of the box characterizes the number of features, and the height characterizes the size of the feature map. According to the geographical area selected for the study in this paper, the size of the input feature image for the semantic segmentation network part in PrecipGradeNet is 129×249 pixels. In the encoder part, the 3×3 convolutional layer (gray arrow) is used to expand the 8 feature channels of external input to 64 features with the same feature map size, the 1×1 convolution (red arrow) is used to halve the number of features to generate layer shortcut with the same feature map size, and the Resblock (blue arrow) is used to double the number of features and halve the feature map size. In the decoder part, convT Resblock (green arrow, replace the convolution layer of Resblock with the deconvolution layer) is used to change the number of features to 1/4 of the original number and double the size of the feature map. The layer shortcut (purple arrow) is concatenated with the deconvolved feature map and used as the input of the next layer of deconvolution Resblock. Finally, the probability output of 11 precipitation grades is obtained by the 3×3 convolution layer, and then the category with the highest probability for each pixel is obtained by the argmax function to get the final predicted precipitation grade. It is worth mentioning that Cross Entropy Loss (CEL) is used in the network. Since the proportion of different precipitation classes in the image varies greatly, the weight of precipitation classes is added to CEL to balance its influence on the model, and the weight is inversely proportional to the number of pixels corresponding to the precipitation grades.

After the completion of the semantic segmentation, the semantic segmentation results are fed into the regression network with the IR features to obtain the QPE. To make the precipitation rate regression network focus more on the strong precipitation image elements and balance the influence of a larger number of light precipitation image elements, an additional layer of 3×3 maxfiltered precipitation grades is added to the segmentation results to improve the influence of strong precipitation. The structure of the regression network is similar to the semantic segmentation network. However, the input becomes 10 layers (8 layers of IR features + 1 layer of precipitation level segmentation results + 1 layer of maximum filter layer). The output becomes 1 layer, which is QPE. The network depth reduces to 2 layers, and the Loss function is MSEloss.

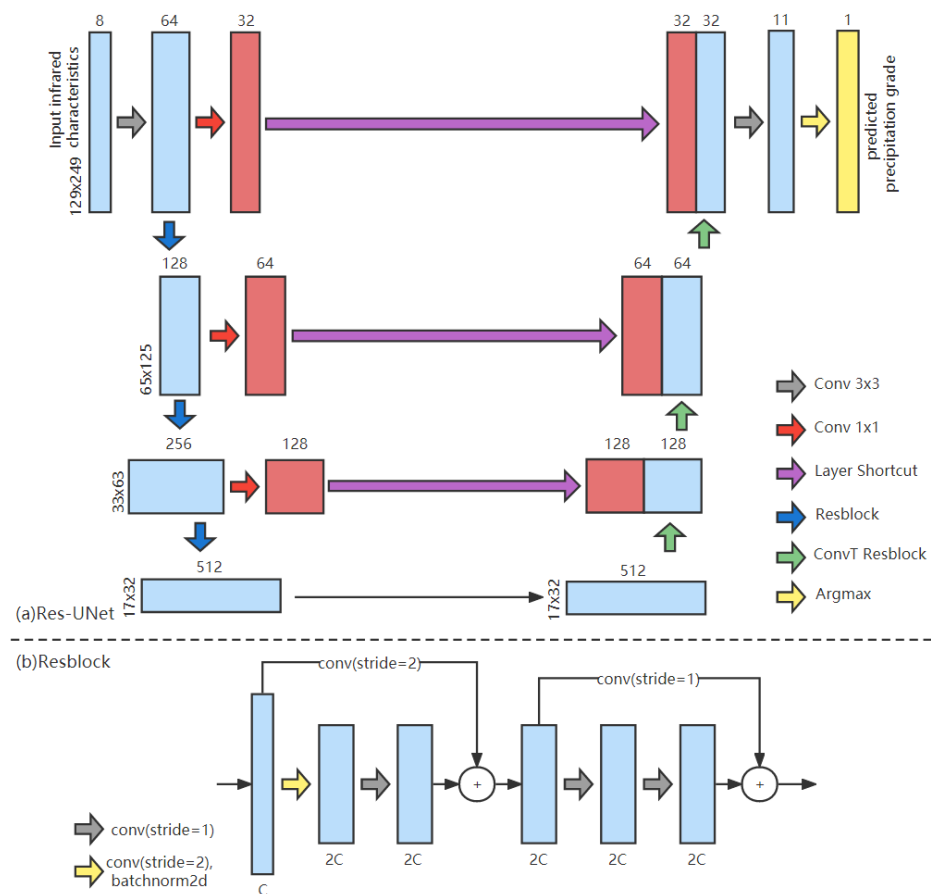


Figure 4. Construction of Res-UNet and Resblock. (a) Network construction of Res-UNet as semantic segmentation network in PrecipGradeNet. (b) Construction of Resblock; C refers to the number of input channels.

4. Experiment

According to the flow chart of method shown in Figure 2, the experimental process is divided into data pre-processing, dataset construction, construction, deployment, and training of the two models.

4.1. Data Preprocessing

Before the experiment, it was necessary to pre-process the input data of the model. The main work was as follows. First, the spatial resolution differences of different data need to be eliminated. The spatial resolution of the PMW precipitation fusion product IMERG is $0.1^\circ \times 0.1^\circ$ (about $10 \text{ km} \times 10 \text{ km}$), and the spatial resolution of FY-4A L1 FDI and FY-4A L2 QPE is about 4 km. In order to ensure the consistency of the spatial resolution and to avoid the inferred values in up-sampling IMERG data from affecting the quality of the data as the true value, the FDI/QPE data on the $0.1^\circ \times 0.1^\circ$ grid were weighted by the original image elements within the grid, and the weight was inversely proportional to the distance to the interpolation center. Second, it was necessary to eliminate the variability in the observation time. The observation time of each image element was recorded in the IMERG data to the minute, and the corresponding image elements were filtered in the IMERG data according to the 15-min observation period of each FDI/QPE data point in this paper. Finally, the FDI data were transformed into different infrared features according to Table 4.

As the IMERG data product is already an equal latitude and longitude grid at the acquisition stage, which requires no spatial projection processing, the IMERG data can be used after the image element filtered above. The IMERG precipitation grades data and maxfiltered grades data are obtained using the observation time filtered IMERG data.

4.2. Dataset Construction

The data collected in this paper include FY-4A L1 FDI data, FY-4A L2 QPE data, and IMERG Early data.

The datasets for training and validation of PrecipGradeNet were obtained using the pre-processed FY-4A L1 FDI and IMERG data. The input dataset for semantic segmentation network in PrecipGradeNet is FY-4A L1 FDI data, and the target is the IMERG precipitation level. The input dataset for the regression network in PrecipGradeNet is FY-4A L1 FDI data, IMERG precipitation grades, and maxfiltered IMERG precipitation grades, and the target is the IMERG precipitation rate. The first 9/10 data of the dataset was used for training of the network, and the last 1/10 data was used for validation of the network and determining when to stop the training. The dataset for semantic segmentation network training can be obtained by intercepting the first 9 layers of data (8 layers of FY-4A L1 FDI data, 1 layer of IMERG precipitation level) from the dataset for regression network training.

The dataset used for application testing of PrecipGradeNet adds FY-4A L2 QPE data to the FY-4A L1 FDI and IMERG data as a comparison for application effectiveness.

4.3. Model Construction, Deployment, and Training

The semantic segmentation network and the regression network of PrecipGradeNet were trained separately using the corresponding datasets until the best results were obtained, and finally, the semantic segmentation network and the regression network were combined to obtain the complete PrecipGradeNet. The semantic segmentation network and the regression network both use the SGD optimizer and the cosine annealing algorithm to adjust the learning rate with an initial learning rate of 1×10^{-5} and a training batch size of 40. The semantic segmentation network uses Cross Entropy Loss as the loss function and the regression network uses MSELoss as the loss function.

4.4. Evaluation Metrics

This paper evaluates the retrieval of PrecipGradeNet in three aspects: precipitation fall area identification, precipitation intensity interval discrimination, and precipitation quantification accuracy. The classification indexes are used to evaluate the effectiveness of precipitation fall zone identification and precipitation intensity interval discrimination, including probability of detection (POD), false alarm rate (FAR), critical success index (CSI), and Heidke skill score (HSS). The POD reflects the sensitivity of the retrieval method to precipitation while the FAR represents the probability that the retrieval method misjudges precipitation, and the HSS and CSI are comprehensive evaluation indicators that consider both correct and incorrect. The regression indicators are used to evaluate the quantitative retrieval of precipitation, including root mean square error (RMSE) and Pearson correlation coefficient (CC), as defined in Table 6.

4.5. Testing Set Validation

After testing with the validation set that is independent of the training set of time, the results of IMERG compared with PrecipGradeNet output QPE were obtained, as shown in Figure 5. Figure 5a is the IMERG precipitation data as the training target, and Figure 5b is the precipitation rate of PrecipGradeNet output. From this Figure, we can see the high similarity between IMERG precipitation and PrecipGradeNet output precipitation. In addition, we can find that some small and light precipitation areas in IMERG precipitation images are not detected by PrecipGradeNet, indicating that PrecipGradeNet may not be accurate in capturing light precipitation features in a very small spatial area, but in general, PrecipGradeNet still has a certain degree of accuracy. Table 7 lists the error indices or error parameters in the validation periods. The trained PrecipGradeNet has an RMSE of 0.34 and a POD of 0.79, which has been able to retrieve the precipitation rate with some accuracy.

Table 6. Description of the indicators. TT represents the pixel number of true positive, TF represents the pixel number of false positive, FF represents the pixel number of true negative, FT represents the pixel number of detection failure; y_i is the truth, and \hat{y}_i is the estimation. “Optimum” indicates the best value for the indicators.

Indicators	Definition	Optimum
POD	$\frac{TT}{TT + FT}$	1
FAR	$\frac{TF}{TT + TF}$	0
CSI	$\frac{TT}{TT + TF + FT}$	1
HSS	$2 \frac{TT * FF - TF * FT}{[(TT + FT) * (FT + FF) + (TT + TF) * (TF + FF)]}$	1
RMSE	$\frac{1}{N} \sum_{i=1}^N \sqrt{(\hat{y}_i - y_i)^2}$	0
CC	$\frac{\frac{1}{N} \sum_{i=1}^N (\hat{y}_i - \bar{\hat{y}})(y_i - \bar{y})}{S_{\hat{y}} \cdot S_y}$	1

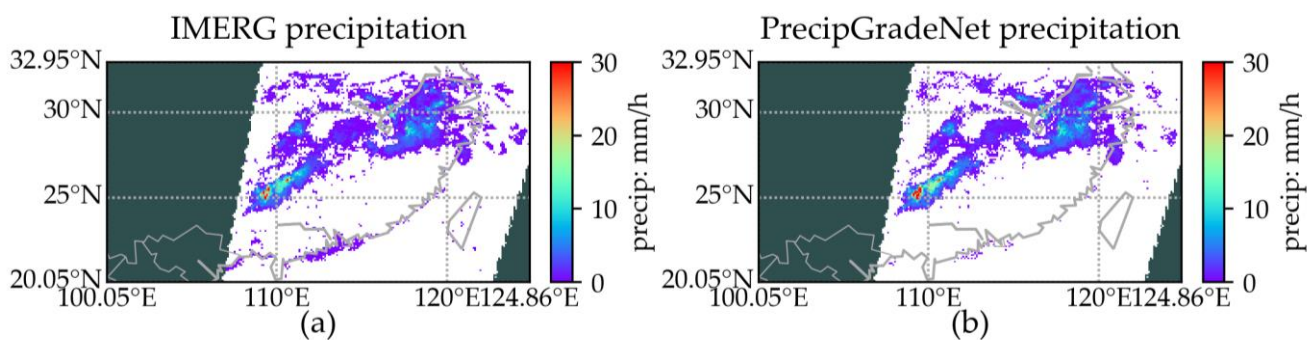


Figure 5. Comparison between IMERG precipitation data and PrecipGradeNet output during validation period. (a) precipitation of IMERG. (b) precipitation output by PrecipGradeNet.

Table 7. Indexes between PrecipGradeNet estimation and IMERG in validation results of model training during 3 July 2021 to 11 July 2021, total 1,534,798 pixels.

POD	FAR	CSI	HSS	RMSE	CC
0.79	0.35	0.56	0.64	0.34	0.65

5. Evaluation and Application

In this paper, the performance of PrecipGradeNet was evaluated by validation sets during the training process and deciding when to stop the model training based on the results. After the model training was completed, the retrieval of PrecipGradeNet was evaluated with IMERG data by comparison to FY-4A L2 QPE data in August–October 2021. The FY-4A L1 FDI data from August–October 2021, which was used as the data of the comparison period, had a total of 838 images after excluding the data with more than 90% weight of null data, and totally 3,370,943 pixels. The metrics for the comparative evaluation of application effects were the same as those for the validation phase.

5.1. Quantitative Accuracy Evaluation

5.1.1. Falling Area Recognition

The comparison of the detection effect of PrecipGradeNet and FY-4A QPE products on precipitation area is shown in Table 8. The POD performance of PrecipGradeNet in falling area recognition has nearly 50% improvement compared with FY-4A QPE product, while the FAR has decreased by about 30%. The CSI and HSS metrics in falling area recognition, which comprehensively evaluate the overall effectiveness, improved by 21% and 14%, respectively. The results indicate the superiority of PrecipGradeNet in precipitation area identification.

Table 8. Comparison of the effect of the PrecipGradeNet and FY-4A L2 QPE for falling area recognition during the evaluation period of 4 August 2021 to 7 October 2021, total 3,370,943 pixels.

	POD	FAR	CSI	HSS
PrecipGradeNet	0.58	0.43	0.4	0.47
FY-4A L2 QPE	0.39	0.33	0.33	0.41
Improve Rate	48.72%	−30.30%	21.21%	14.63%

5.1.2. Intensity Intervals Classification

The common precipitation intensity interval criteria classify precipitation intensity into three categories, as shown in Table 2. We segmented precipitation estimated by PrecipGradeNet, FY-4A L2 QPE, and IMERG precipitation into three precipitation intensity intervals according to the criteria in Table 2 and compared the indexes for the different intervals. A comparison of the detection effects of PrecipGradeNet QPE and FY-4A L2 QPE on precipitation intervals classification is shown in Table 9. The detection accuracy of PrecipGradeNet is higher than that of FY-4A L2 QPE for light precipitation as the majority, with POD improved by 114%, FAR roughly equal, and CSI and HSS improved by 64% and 52%, respectively. Compared with the FY-4A L2 QPE product, PrecipGradeNet has higher POD and lower FAR for medium precipitation with higher detection capability. In contrast, both POD and FAR of FY-4A L2 QPE for heavy precipitation are higher, which was caused by its overflow in judging the area of heavy precipitation.

Table 9. Summary of the PrecipGradeNet and FY-4A L2 QPE detection performance for different precipitation intensity intervals during the evaluation period of 4 August 2021 to 7 October 2021, total 3,370,943 pixels.

	PrecipGradeNet				FY-4A L2 QPE			
	POD	FAR	CSI	HSS	POD	FAR	CSI	HSS
No rain	0.89	0.10	0.81	0.47	0.95	0.13	0.83	0.41
Light rain	0.45	0.57	0.28	0.32	0.21	0.54	0.17	0.21
Moderate rain	0.28	0.73	0.16	0.26	0.24	0.79	0.13	0.20
Heavy rain	0.12	0.78	0.09	0.15	0.37	0.81	0.14	0.25

Considering that the pixel share of heavy precipitation is relatively small, the point-to-point detection accuracy is influenced by the location, and especially the heavy precipitation with fewer pixels is influenced by the location more than the intensity. A comparison of the effect of extending the detection accuracy to one precipitation intensity interval is shown in Table 10. In this statistic, the discrimination error of the precipitation interval is considered to be correct within 1 precipitation intensity interval, where no precipitation and light precipitation are mutually exclusive.

Table 10. Summary of the PrecipGradeNet and FY-4A L2 QPE detection performance for different precipitation intensity intervals during the evaluation period of 4 August 2021 to 7 October 2021, total 3,370,943 pixels. (Error within one precipitation intensity interval).

	PrecipGradeNet				FY-4A L2 QPE			
	POD	FAR	CSI	HSS	POD	FAR	CSI	HSS
No rain	0.89	0.10	0.81	0.47	0.95	0.13	0.83	0.41
Light rain	0.56	0.47	0.37	0.44	0.32	0.39	0.27	0.34
Moderate rain	0.58	0.43	0.40	0.47	0.39	0.33	0.33	0.41
Heavy rain	0.37	0.61	0.24	0.36	0.45	0.66	0.24	0.37

As shown in Table 10, after extending one precipitation intensity interval, the CSI and HSS of the two models are roughly equal in the heavy precipitation interval, while the light and moderate precipitation detection ability of PrecipGradeNet is still higher than that of FY-4A L2 QPE. This indicates that PrecipGradeNet has probed the approximate geographical range of strong precipitation. PrecipGradeNet has a low POD value for heavy precipitation due to the low coverage of heavy precipitation and the high influence of location, which we will give an in-depth analysis in the next subsection.

5.1.3. Precipitation Intensity

Table 11 provides the quantitative precipitation retrieval performance of PrecipGradeNet versus FY-4A L2 QPE. Compared with the FY-4A L2 QPE product, PrecipGradeNet improved over FY-4A L2 QPE in all metrics of precipitation intensity accuracy, with an RMSE of 1.91 mm/h, 16% lower than FY-4A L2 QPE, and a CC of 0.38, 15% better than FY-4A L2 QPE. This indicates that PrecipGradeNet is better than FY-4A L2 QPE in terms of both absolute difference in quantity and linear correlation, demonstrating the superior performance of PrecipGradeNet in quantitative precipitation retrieval.

Table 11. Comparison of the precipitation intensity accuracy of the PrecipGradeNet and FY-4A L2 QPE.

	PrecipGradeNet	FY-4A L2 QPE	Improvement Rate
RMSE	1.91	2.27	15.86%
CC	0.38	0.33	15.15%

Figure 6 shows the heat map between the results of PrecipGradeNet retrieval, FY-4A L2 QPE products and IMERG. Two forms of heat maps are used with general linear coordinates and logarithmic coordinates, which can better observe the relative errors. The precipitation intensity interval of Figure 6a,c is 0.5 mm/h, and Figure 6b,d have a total of 150 pixels in each X/Y axis. Figure 6a,c is in linear coordinates and Figure 6b,d is in logarithmic coordinates. Figure 6b,d shows that most of the precipitation is distributed between 0–10 mm, with the most concentrated area in the range of 1–5 mm. Figure 6b shows that there are some pixels in the interval of 10–15 mm/h for IMERG and 0–5 mm/h for PrecipGradeNet, which indicates some underestimation of PrecipGradeNet in the medium precipitation interval. Figure 6c shows that most of the precipitation pixels of FY-4A L2 QPE and IMERG are distributed in the interval of IMERG <10 mm/h and FY-4A L2 QPE <15 mm/h. This shows that the precipitation of FY-4A L2 QPE tends to shift toward the heavy precipitation, and we find that the FY-4A L2 QPE has many pixels on the 20-mm dividing line. As compared to Figure 6a, the PrecipGradeNet does not show a shift toward light precipitation [26] or a shift toward heavy precipitation. The overall performance tests demonstrated the ability of PrecipGradeNet to more accurately and unbiasedly fit precipitation quantitatively.

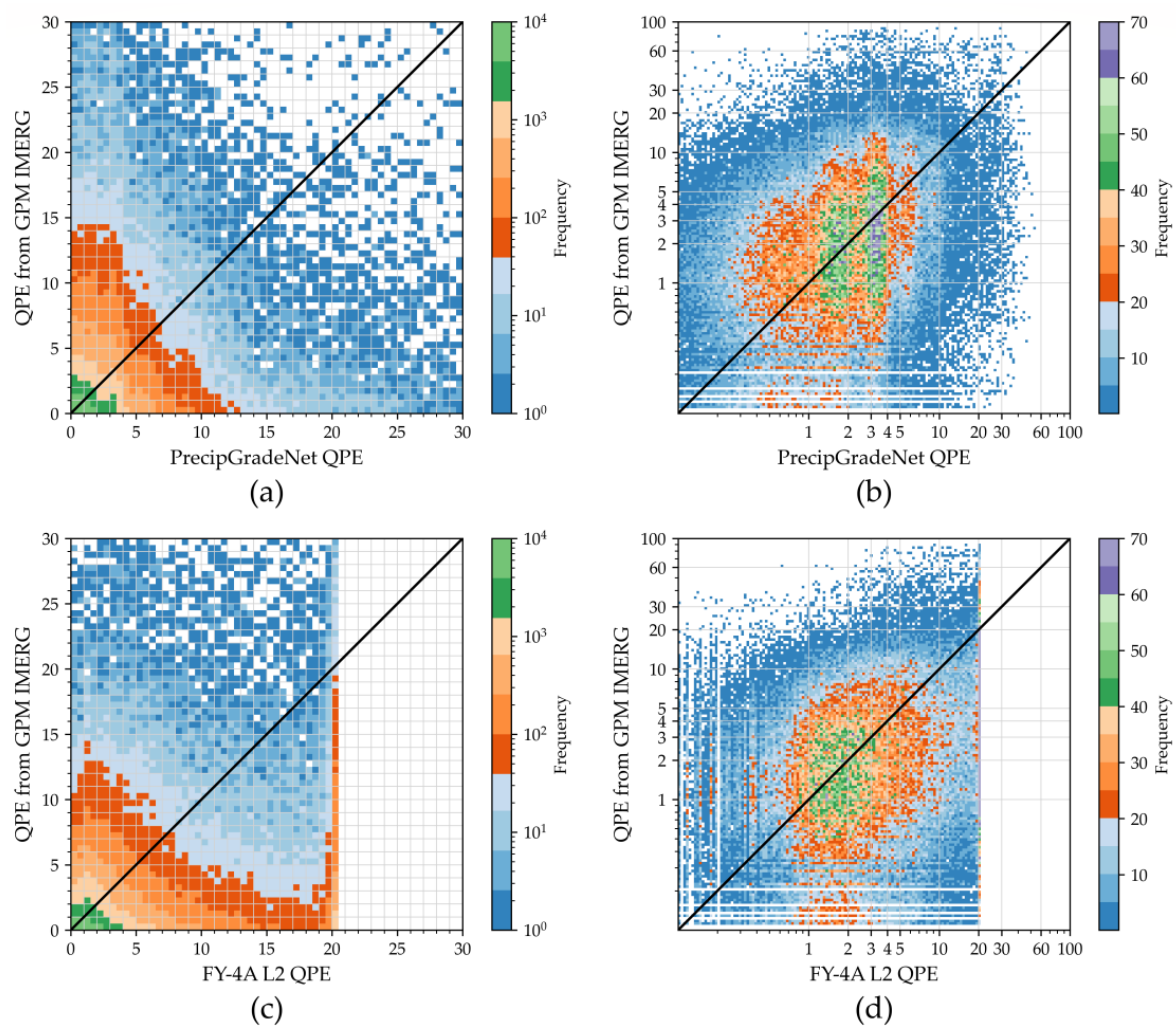


Figure 6. Relationship between PrecipGradeNet precipitation, FY-4A QPE and IMERG precipitation during the test period (from 4 August 2021 to 7 October 2021), with linear axis and logarithmic axis. (a) Histogram between precipitation from PrecipGradeNet and IMERG; (b) histogram between precipitation from PrecipGradeNet and IMERG in logarithmic scale; (c) histogram between precipitation from FY-4A L2 QPE and IMERG; (d) histogram between precipitation from FY-4A L2 QPE and IMERG in logarithmic scale.)

Figure 7 shows the maps of RMSE and CC variation with spatial location between PrecipGradeNet prediction results, FY-4A QPE, and IMERG. As shown by the comparison of Figure 7a,b, the RMSE of PrecipGradeNet prediction with IMERG is lower than the RMSE of FY-4A L2 QPE in most regions. In addition, the RMSEs of both PrecipGradeNet and FY-4A L2 QPE show a higher RMSE on ocean than on land, suggesting that the precipitation characteristics on ocean may be different from those on land. Comparison of Figure 7c,d shows that the high value of CC (green) of PrecipGradeNet prediction results compared with FY-4A L2 QPE pattern is more dispersed, with a wider distribution over land and lower only in coastal offshore areas, while the part with low CC (blue) is less, and the overall effect is steadily maintained at a medium-high level. The partial image comparison of CC from Figure 7f shows that FY-4A L2 QPE has more CC < 0 (white) areas in this region, which means that the retrieval results are negatively correlated with the true value, and it is relatively rare in the PrecipGradeNet results. In summary, compared with the FY-4A L2 QPE product, the RMSE of PrecipGradeNet improves throughout the land and sea regions, while the CC is significantly improved in the land region and avoids most of the negative

correlations at sea. The overall performance shows that PrecipGradeNet is able to estimate precipitation more accurately in quantitative terms compared to FY-4A L2 QPE.

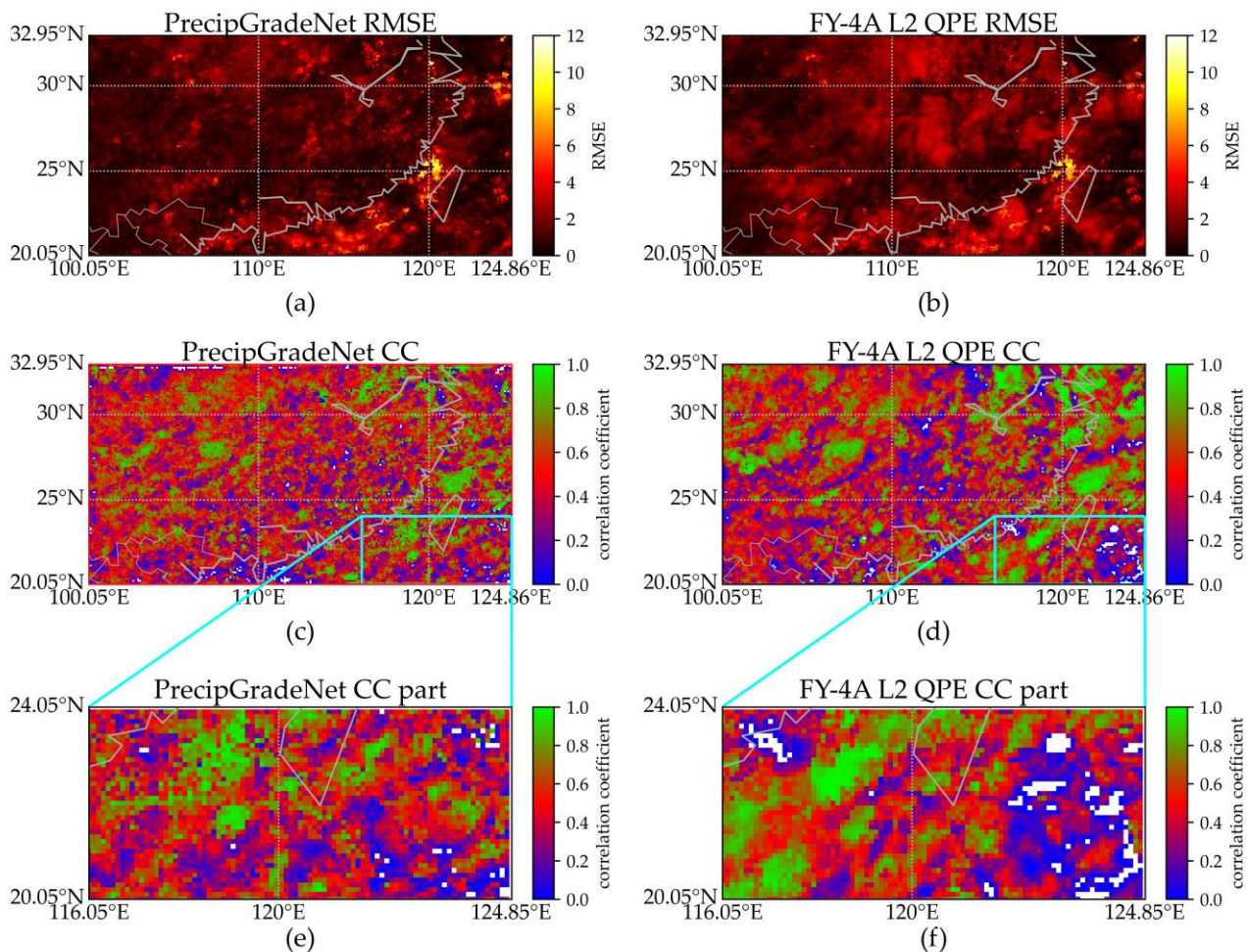


Figure 7. The Root Mean Square Error (RMSE) and Pearson correlation coefficient (CC) map for the FY-4A L2 QPE and PrecipGradeNet during the test period (from 4 August 2021 to 7 October 2021). (a) RMSE between the prediction of PrecipGradeNet and IMERG. (b) RMSE between the FY-4A L2 QPE and IMERG. (c) CC between the prediction of PrecipGradeNet and IMERG. (d) CC between the FY-4A L2 QPE and IMERG (e) part of (c) at 20°N–24°N, 106°E–125°E. (f) part of (d) at 20°N–24°N, 106°E–125°E.

The quantitative accuracy indicators of precipitation retrieval, RMSE and CC, and the classification indicators, POD and FAR, are all point-to-point intensity comparisons. Apart from intensity, they are also related to the spatial relationship between precipitation areas. Especially in the heavy precipitation area covering a small region, the accuracy of the spatial location of the precipitation area often has a greater impact on the RMSE metrics than the difference in precipitation intensity. In the most extreme case, the heavy precipitation intensity is accurate while the spatial location has a slight difference, which can have a doubled negative impact on the RMSE. In some cases, the RMSE indicator of heavy precipitation features detected is worse than that of no heavy precipitation detected, which suggests that more indicators are needed to evaluate the quantitative effect of precipitation retrieval in this paper. The frequency distribution map of precipitation intensity can reflect the frequency distribution of different precipitation intensities in different models and products, and this indicator can more accurately reflect the intensity of precipitation rather than the influence of spatial location and evaluate the effect of strong precipitation more accurately.

Figure 8 reflects the intensity frequency distribution of PrecipGradeNet retrieval precipitation, FY-4A QPE product precipitation, and IMERG precipitation in different intensity intervals. Figure 8a has a total of 200 binaries, and Figure 8b–e have 100 binaries each. Figure 8a shows that there is a spike at 20 mm/h in the FY-4A L2 QPE product, which indicates that there is overflow in the detection of heavy precipitation by the FY-4A L2 QPE. Figure 8a,b shows that there are more missing cases in the discrimination of the light precipitation by FY-4A L2 QPE, while this does not happen in PrecipGradeNet. Figure 8c shows that the number of pixels discerned by PrecipGradeNet and FY-4A L2 QPE in the medium precipitation interval is approximately the same, with some underestimate by PrecipGradeNet and some overestimate by FY-4A L2 QPE. Figure 8d shows that in the lower part of the high precipitation, PrecipGradeNet is a bit underestimated and FY-4A L2 QPE is a bit overestimated. Figure 8e shows that the number of heavy precipitation pixels retrieved by PrecipGradeNet is closer to that of IMERG.

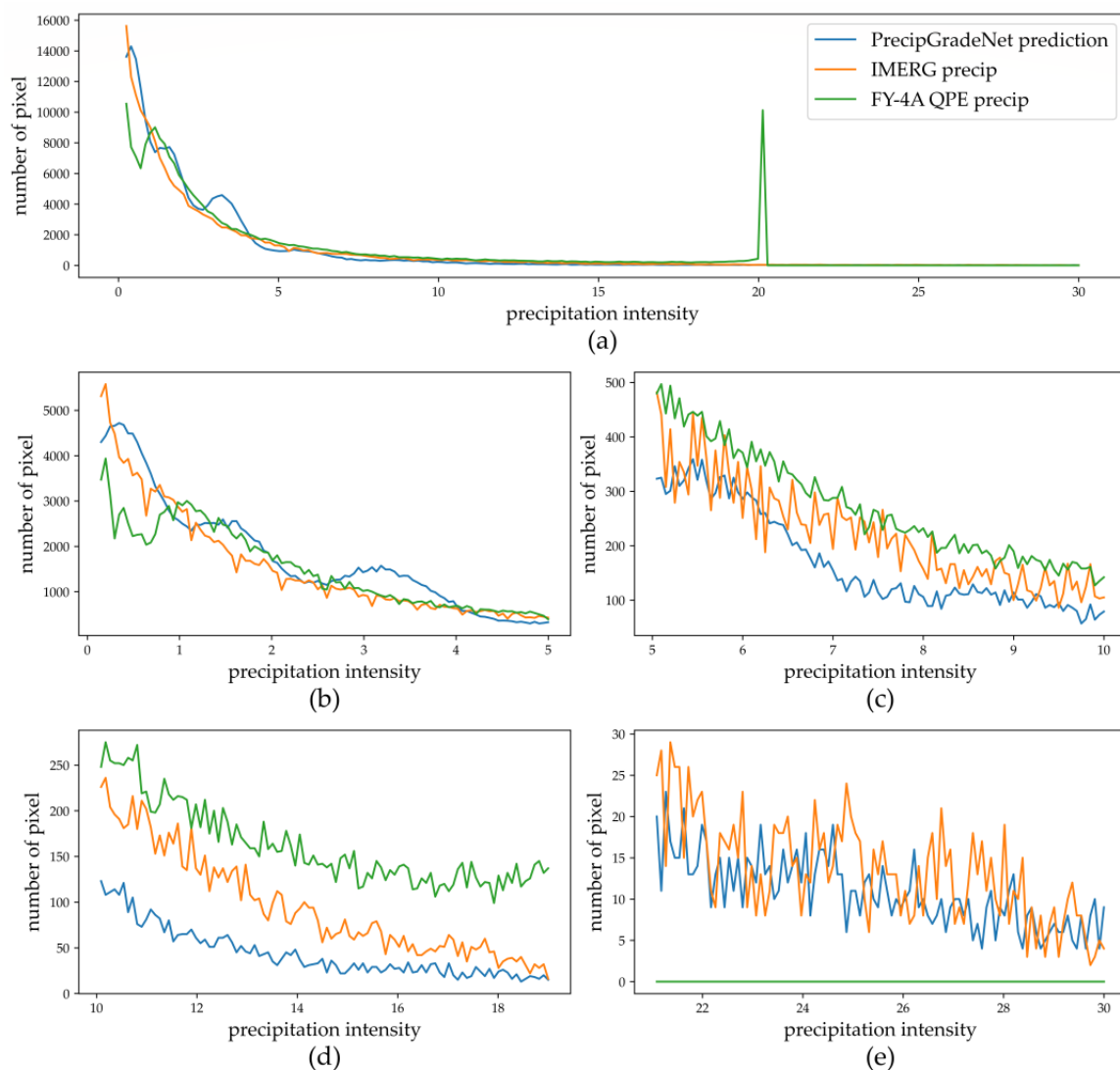


Figure 8. Line graph of precipitation intensity frequency distribution of 3 kinds of QPE by different scales during the test period (from 4 August 2021 to 7 October 2021). (a) Line graph of precipitation all between 0–30 mm/h. (b) Line graph of precipitation between 1–5 mm/h. (c) Line graph of precipitation between 5–10 mm/h. (d) Line graph of precipitation between 10–19 mm/h. (e) Line graph of precipitation between 21–30 mm/h.

5.2. Case Study

As mentioned in various studies on IR bright-temperature retrieval of precipitation, different experimental procedures of schemes for infrared brightness temperature precipitation retrieval have encountered varying degrees of underestimation of precipitation under very heavy precipitation [10,19,25] and overflow of heavy precipitation determination [14,15], as well as missing [26] or overestimation [27] of light precipitation. In order to demonstrate the performance of the PrecipGradeNet for light precipitation and very heavy precipitation, data containing only light precipitation in the application dataset were selected for analysis. As a supplement, a case with a large area of light precipitation and a case with a small area of heavy precipitation were selected to demonstrate the application effect.

5.2.1. Light Precipitation

In order to evaluate the effectiveness of PrecipGradeNet for light precipitation, the data with the maximum precipitation rate of IMERG exceeding 8 mm/h in the dataset were excluded; only those with medium and low precipitation were retained. The pixels judged as precipitation rate >8 mm/h in these data by PrecipGradeNet and FY-4A L2 QPE were treated as 8 mm/h. Figure 9 shows the frequency distribution curves of precipitation rate obtained using the light precipitation dataset. Figure 9a shows that FY-4A L2 QPE still has a large number of cases where precipitation is judged as heavy precipitation in the light precipitation cases, while this phenomenon is significantly less in PrecipGradeNet. This shows a strong tendency of FY-4A L2 QPE to overestimate precipitation in light precipitation cases. Figure 9b,c shows no significant difference in the frequency distribution of the precipitation rate between PrecipGradeNet, FY-4A L2 QPE, and IMERG in the light precipitation interval.

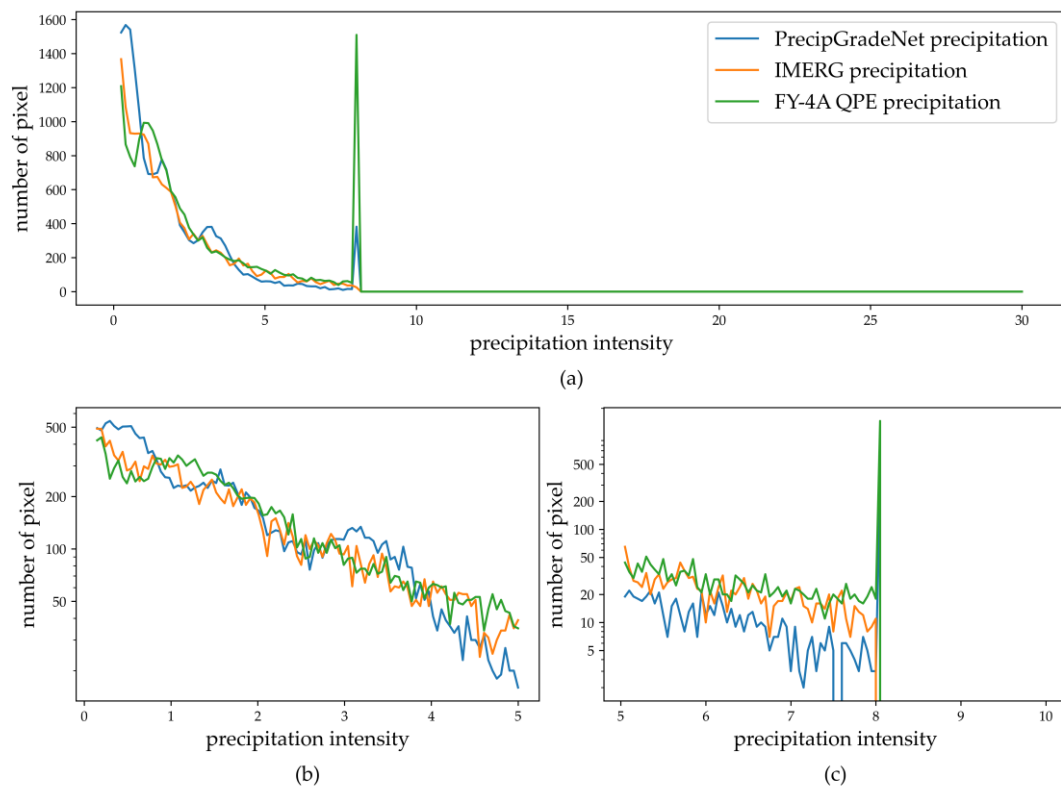


Figure 9. Line graph of precipitation intensity frequency distribution of 3 kinds of QPE in low precipitation dataset by different scales during the test period (from 4 August 2021 to 7 October 2021). (a) Line graph of precipitation all between 0–30 mm/h. (b) Line graph of precipitation between 1–5 mm/h. (c) Line graph of precipitation between 5–10 mm/h.

Table 12 shows the comparison of light precipitation retrieval using a light precipitation dataset with a complete precipitation dataset. The application effect of both PrecipGradeNet and FY-4A L2 QPE in the simply light precipitation dataset decreases compared with the complete precipitation dataset, while PrecipGradeNet has 111% higher POD, 22% worse FAR, 60% higher CSI, and 43% higher HSS than FY-4A L2 QPE in the simply light precipitation process. The overall retrieval of PrecipGradeNet for light precipitation processes is still better than that of FY-4A L2 QPE, while the retrieval of the dataset without strong precipitation processes is lower than that of the complete dataset, reflecting that PrecipGradeNet has better retrieval for convective precipitation (which usually has strong precipitation areas) than stratified precipitation (which usually does not have strong precipitation areas).

Table 12. Summary of the PrecipGradeNet and FY-4A L2 QPE detection performance of light rain in light rain dataset and full dataset.

	PrecipGradeNet				FY-4A L2 QPE			
	POD	FAR	CSI	HSS	POD	FAR	CSI	HSS
Light rain–light rain dataset	0.38	0.6	0.24	0.33	0.18	0.49	0.15	0.23
Light rain–full dataset	0.45	0.57	0.28	0.32	0.21	0.54	0.17	0.21

Figure 10 is a comparative display of the precipitation retrieval for a large area of light precipitation, and the data was acquired on 2022-05-02T13:00:00 UTC. From the comparison of Figure 10b,d, it shows that PrecipGradeNet has higher accuracy in discerning light precipitation over a large area, and the coverage is basically the same; however, the precipitation estimated by PrecipGradeNet under light precipitation conditions is lower than that of IMERG. From Figure 10a,c, although the coverage varies, relatively strong features in the light precipitation area could also be captured by the semantic segmentation network. This feature was retained in the result, making the detection performance of PrecipGradeNet for light precipitation higher. However, at the same time, similar to the results we obtained in Figure 5, PrecipGradeNet has some degree of underestimation in the medium precipitation interval. From Figure 10d,f, we can see that the recognition rate of FY-4A L2 QPE for large-scale light precipitation is lower than that of PrecipGradeNet, and the recognition range for large-scale light precipitation is smaller, with many missing cases. This indicates that PrecipGradeNet is better than FY-4A L2 QPE in retrieving light precipitation over a large area. From Figure 10h,i, we can see that the difference between precipitation predicted by PrecipGradeNet and IMERG precipitation is smaller than that between FY-4A L2 QPE and IMERG precipitation. This indicates that the precipitation predicted by PrecipGradeNet is closer to the precipitation characteristics obtained by PMW data.

5.2.2. Heavy Precipitation

Figure 11 shows the comparison of different QPEs for an individual case of heavy local precipitation, acquired on 2021-09-19T02:45:00 UTC. In this case, the maximum precipitation rate of IMERG is 27.3 mm/h, and the center of heavy precipitation is near 110°E, 30°N. Figure 11b,d shows that PrecipGradeNet is more accurate in locating the center of heavy precipitation as compared to IMERG. Figure 11e,f shows that although FY-4A L2 QPE detected heavy precipitation, it could not accurately locate the center of heavy precipitation. There was a serious overflow phenomenon for the determination of heavy precipitation, and some areas that have no high precipitation intensity were determined as heavy precipitation areas, which is similar to the feature pattern in feature 8, as Figure 11g shows, indicating that the FY-4A L2 QPE only detects shallow features in the IR, which is less accurate than PrecipGradeNet in terms of feature accuracy. From Figure 11h, it can be seen that there is a dark blue (predicted precipitation < IMERG precipitation) area next to the dark red (predicted precipitation > IMERG precipitation) area in the center of heavy

precipitation (110°E , 30°N). Figure 11b,d showed that the precipitation intensity at the center of heavy precipitation judged by PrecipGradeNet is very little different from the IMERG precipitation: there is only a slight difference in the location of the judged center of heavy precipitation as compared to IMERG, which causes an unexpected decrease in RMSE in Section 5.1.3. Therefore, the frequency distribution graph is used to supplement the evaluation of the high precipitation performance of PrecipGradeNet in Figure 8. Figure 11i shows that FY-4A L2 QPE has a significant tendency to overestimate the intensity and spatial extent of high precipitation, which does not appear in the retrieval results of Figure 11h by PrecipGradeNet as compared to IMERG. This indicates that PrecipGradeNet is more accurate than FY-4A L2 QPE in determining the spatial extent, location, and intensity of high-intensity precipitation.

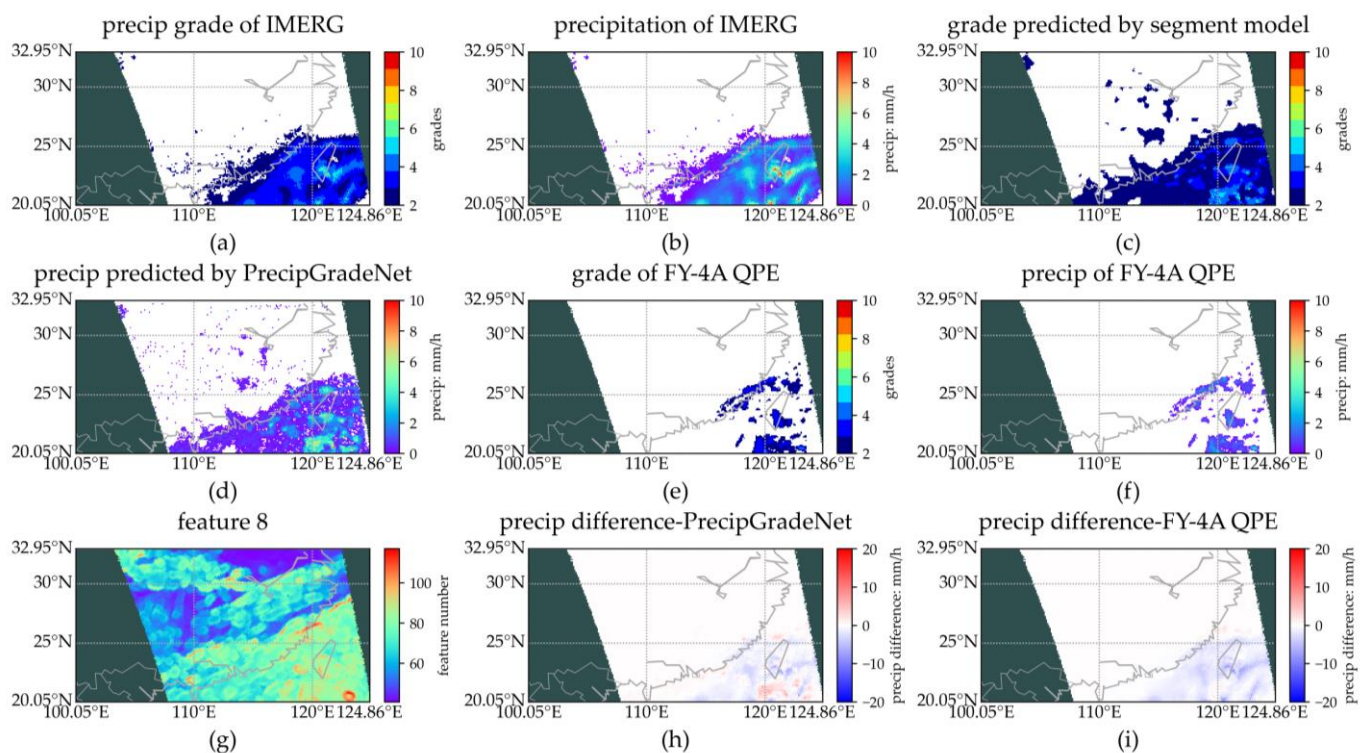


Figure 10. Comparison of precipitation grade and precipitation of IMERG, retrieval model, and FY-4A L2 QPE during 2022-05-02T13:00:00 UTC ((a) precipitation grade of IMERG; (b) precipitation of IMERG; (c) grade predicted by segment model of PrecipGradeNet; (d) precipitation predicted by PrecipGradeNet; (e) precipitation grade of FY-4A L2 QPE; (f) precipitation of FY-4A L2 QPE; (g) the feature 8 brightness temperature different; (h) precipitation difference between PrecipGradeNet estimation and IMERG; (i) precipitation difference between FY-4A L2 QPE and IMERG).

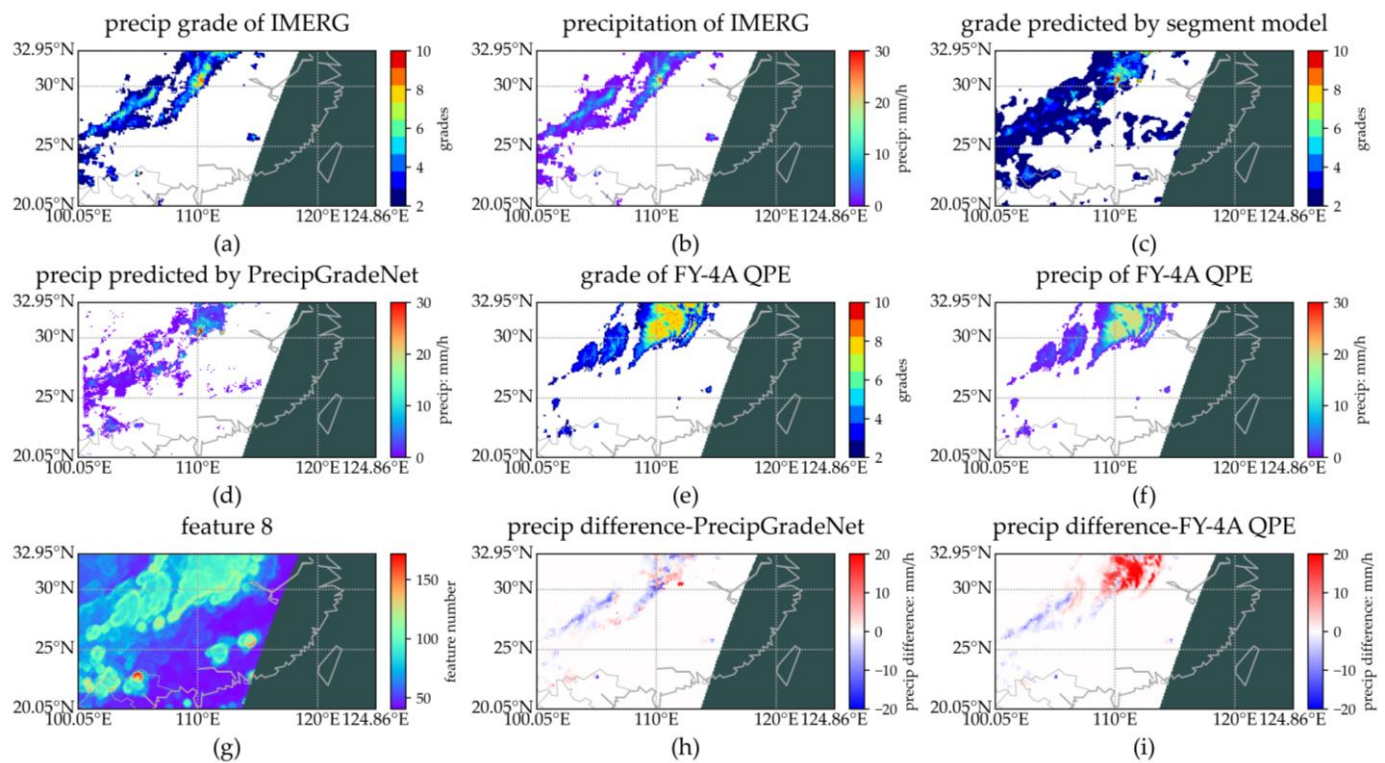


Figure 11. Comparison of precipitation grade and precipitation of IMERG, PrecipGradeNet, and FY-4A L2 QPE during 2021-09-19T02:45:00 UTC ((a) precipitation grade of IMERG; (b) precipitation of IMERG; (c) grade predicted by segment model of PrecipGradeNet; (d) precipitation predicted by PrecipGradeNet; (e) precipitation grade of FY-4A L2 QPE; (f) precipitation of FY-4A L2 QPE; (g) the feature 8 brightness temperature different; (h) precipitation difference between PrecipGradeNet estimation and IMERG; (i) precipitation difference between FY-4A L2 QPE and IMERG).

6. Conclusions

This study proposes a new research method to retrieve the precipitation from optical images for precipitation data in the tropical and subtropical monsoon region of southeastern China with an uneven distribution of intensity amounts. A Res-UNet based DL network called PrecipGradeNet is designed in the geostationary satellite infrared precipitation retrieval algorithm. The algorithm uses a two-step method to segment the precipitation rate and then regresses the precipitation rate quantitatively. By accurately segmenting the precipitation rate grade, it can effectively improve the phenomenon of heavy precipitation overflow and underestimation and more accurately determine the light precipitation areas as compared to IMERG PMW data.

In this paper, the retrieval of PrecipGradeNet is evaluated using the FY-4A L1 FDI, FY-4A L2 QPE, and IMERG data of the same period in August–October 2021 in three aspects, included precipitation fall area identification, precipitation intensity interval discrimination, and precipitation quantification accuracy, and with a focus on the two extreme cases of light and heavy precipitation. The results show that (1) PrecipGradeNet outperforms FY-4A L2 QPE in identifying precipitation fallout areas, with a 48% increase in POD, a 21% increase in CSI, and a 14% increase in HSS; (2) PrecipGradeNet improves POD by 114%, CSI and HSS by 64% and 52%, respectively, for light precipitation compared to FY-4A L2 QPE; (3) The CSI and HSS of PrecipGradeNet for strong precipitation are the same as those of FY-4A L2 QPE, but PrecipGradeNet has no overflow for heavy precipitation, and the intensity distribution is closer to IMERG in the region of high intensity precipitation above 20 mm; (4) the quantitative performance indexes RMSE and CC of PrecipGradeNet are 16% and 15% higher than those of FY-4A L2 QPE. The accuracy of PrecipGradeNet is

higher than that of FY-4A L2 QPE in both large area of light precipitation and small area of heavy precipitation.

Compared with the traditional ML method for retrieving QPEs [39], PrecipGradeNet maintains the sensitivity of discrimination for light precipitation while accurately detecting areas of heavy precipitation due to the inclusion of semantic segmentation of different precipitation grades in the retrieval process. Experiments show that PrecipGradeNet has superior performance in both low and extreme high precipitation conditions.

In the future, we can extend this algorithm to a global scale and train PrecipGradeNet on a rolling loop for different months of data to obtain the best performance. We can also introduce data on land–sea relationships or topography to make the model applicable to complex land–sea relationships and topography and introduce more advanced DL models to improve the performance of PrecipGradeNet in order to make the model a practical product.

Author Contributions: Conceptualization, D.Z., Y.H. and N.X.; methodology, D.Z. and Y.H.; software, D.Z.; validation, D.Z.; formal analysis, D.Z., N.X. and X.L.; investigation, D.Z., N.X. and X.L.; resources, Y.H.; data curation, D.Z., N.X. and X.L.; writing—original draft preparation, D.Z.; writing—review and editing, N.X., Y.H. and X.L.; visualization, D.Z. and L.Z.; supervision, Y.H. and N.X.; project administration, D.Z.; funding acquisition, N.X. and Y.H. All authors have read and agreed to the published version of the manuscript.

Funding: This research was funded by the National Key R&D Program of China, grant number 2018YFB0504800, 2018YFB0504802 and 2018YFB0504900, and the National Natural Science Foundation of China, grant number 42175167.

Data Availability Statement: The IMERG data used in this paper was obtained from NASA’s Global Precipitation Measurement and are available at <https://jsimpsonhttps.pps.eosdis.nasa.gov/imerg/early/> (accessed on 7 November 2022) with the permission of from NASA’s Global Precipitation Measurement.

Acknowledgments: We would particularly like to acknowledge Benkun Hong in School of Chemistry and Chemical Engineering, Nanjing University for the inspiration of paper writing.

Conflicts of Interest: The funders had no role in the design of the study; in the collection, analyses, or interpretation of data; in the writing of the manuscript; or in the decision to publish the results.

References

- Ding, Y. The variability of the Asian summer monsoon. *J. Meteorol. Soc. Jpn.* **2007**, *85*, 21–54. [[CrossRef](#)]
- Hua, C.; Yihui, D.; Jinhai, H. Reappraisal of Asian Summer Monsoon Indices and the Long-Term Variation of Monsoon. *Acta Meteorol. Sin.* **2007**, *21*, 168–178.
- Ding, Y.; Wang, Z.; Ying, S. Inter-decadal variation of the summer precipitation in East China and its association with decreasing Asian summer monsoon. Part I: Observed evidences. *Int. J. Climatol.* **2008**, *28*, 1139–1161. [[CrossRef](#)]
- Hu, Z.Z.; Nitta, T. Wavelet Analysis of Summer Rainfall over North China and India and SOI Using 1891–1992 Data. *J. Meteorol. Soc. Jpn.* **1996**, *74*, 833–844. [[CrossRef](#)]
- Yu, R.; Zhou, T.; Xiong, A.; Zhu, Y.; Li, J. Diurnal variations of summer precipitation over contiguous China. *Geophys. Res. Lett.* **2007**, *34*, 223–234. [[CrossRef](#)]
- Nitta, T.; Hu, Z.Z. Summer climate variability in China and its association with 500 hPa height and tropical convection. *J. Meteorol. Soc. Jpn.* **2008**, *74*, 425–445. [[CrossRef](#)]
- Hou, A.Y.; Kakar, R.K.; Neeck, S.; Azarbarzin, A.A.; Kummerow, C.D.; Kojima, M.; Oki, R.; Nakamura, K.; Iguchi, T. The Global Precipitation Measurement Mission. *Bull. Am. Meteorol. Soc.* **2014**, *95*, 701–722. [[CrossRef](#)]
- Huffman, G.; Bolvin, D.; Braithwaite, D.; Hsu, K.; Joyce, R.; Kidd, C.; Nelkin, E.; Sorooshian, S.; Tan, J.; Xie, P. *NASA Global Precipitation Measurement (GPM) Integrated Multi-Satellite Retrievals for GPM (IMERG). Algorithm Theoretical Basis Document (ATBD) Version 06*; National Aeronautics and Space Administration (NASA), March: Washington, WA, USA, 2019.
- Huffman, G.J.; Bolvin, D.T.; Nelkin, E.J.; Wolff, D.B.; Adler, R.F.; Gu, G.; Hong, Y.; Bowman, K.P.; Stocker, E.F. *The TRMM Multisatellite Precipitation Analysis (TMPA): Quasi-Global, Multiyear, Combined-Sensor Precipitation Estimates at Fine Scales*; Springer: Dordrecht, The Netherlands, 2007; Volume 8, pp. 38–55. [[CrossRef](#)]
- Joyce, R.J.; Janowiak, J.E.; Arkin, P.A.; Xie, P. CMORPH: A Method that Produces Global Precipitation Estimates from Passive Microwave and Infrared Data at High Spatial and Temporal Resolution. *Am. Meteorol. Soc.* **2004**, *5*, 487–503. [[CrossRef](#)]
- Vicente, G.A.; Scofield, R.A.; Menzel, W.P. The Operational GOES Infrared Rainfall Estimation Technique. *Bull. Am. Meteorol. Soc.* **1998**, *79*, 1883–1898. [[CrossRef](#)]

12. Kuligowski, R.J. A self-calibrating real-time GOES rainfall algorithm for short-term rainfall estimates. *J. Hydrometeorol.* **2002**, *3*, 112–130. [[CrossRef](#)]
13. Thies, B.; Nauss, T.; Bendix, J. Discriminating raining from non-raining cloud areas at mid-latitudes using Meteosat Second Generation SEVIRI day-time data. *Atmos. Chem. Phys.* **2008**, *7*, 219–230. [[CrossRef](#)]
14. Robert, J.; Kuligowski, N.N.S. *GOES-R Advanced Baseline Imager (ABI) Algorithm Theoretical Basis Document for Rainfall Rate (QPE), Version 2.6*; NOAA National Centers for Environmental Information: Asheville, NC, USA, 2013. [[CrossRef](#)]
15. Kühnlein, M.; Appelhans, T.; Thies, B.; Nauss, T. Precipitation Estimates from MSG SEVIRI Daytime, Nighttime, and Twilight Data with Random Forests. *J. Appl. Meteorol. Climatol.* **2014**, *53*, 2457–2480. [[CrossRef](#)]
16. Bellerby, T.; Hsu, K.-l.; Sorooshian, S. LMODEL: A Satellite Precipitation Methodology Using Cloud Development Modeling. Part I: Algorithm Construction and Calibration. *J. Hydrometeorol.* **2009**, *10*, 1081–1095. [[CrossRef](#)]
17. Chen, X.; Huang, W.; Zhao, C.; Tian, Y. Rain Detection From X-Band Marine Radar Images: A Support Vector Machine-Based Approach. *IEEE Trans. Geosci. Remote Sens.* **2020**, *58*, 2115–2123. [[CrossRef](#)]
18. Kühnlein, M.; Appelhans, T.; Thies, B.; Nauss, T. Improving the accuracy of rainfall rates from optical satellite sensors with machine learning—A random forests-based approach applied to MSG SEVIRI. *Remote Sens. Environ.* **2014**, *141*, 129–143. [[CrossRef](#)]
19. Turini, N.; Thies, B.; Horna, N.; Bendix, J. Random forest-based rainfall retrieval for Ecuador using GOES-16 and IMERG-V06 data. *Eur. J. Remote Sens.* **2021**, *54*, 117–139. [[CrossRef](#)]
20. Yuan, Q.; Shen, H.; Li, T.; Li, Z.; Li, S.; Jiang, Y.; Xu, H.; Tan, W.; Yang, Q.; Wang, J.; et al. Deep learning in environmental remote sensing: Achievements and challenges. *Remote Sens. Environ.* **2020**, *241*, 111716. [[CrossRef](#)]
21. Trebing, K.; Stanczyk, T.; Mehrkanoon, S. SmaAt-UNet: Precipitation nowcasting using a small attention-UNet architecture. *Pattern Recognit. Lett.* **2021**, *145*, 178–186. [[CrossRef](#)]
22. Wang, C.; Tang, G.; Gentine, P. PrecipGAN: Merging microwave and infrared data for satellite precipitation estimation using generative adversarial network. *Geophys. Res. Lett.* **2021**, *48*, e2020GL092032. [[CrossRef](#)]
23. Wang, C.; Tang, G.; Xiong, W.; Ma, Z.; Zhu, S. Infrared Precipitation Estimation using Convolutional neural network for FengYun satellites. *J. Hydrol.* **2021**, *603*, 127113. [[CrossRef](#)]
24. Gao, Y.; Guan, J.; Zhang, F.; Wang, X.; Long, Z. Attention-Unet-Based Near-Real-Time Precipitation Estimation from Fengyun-4A Satellite Imageries. *Remote Sens.* **2022**, *14*, 2925. [[CrossRef](#)]
25. Sun, S.; Li, W.; Huang, Y. Retrieval of Precipitation by Using Himawari-8 Infrared Images. *Acta Sci. Nat. Univ. Pekin.* **2019**, *55*, 215–226. [[CrossRef](#)]
26. Min, M.; Bai, C.; Guo, J.; Sun, F.; Liu, C.; Wang, F.; Xu, H.; Tang, S.; Li, B.; Di, D. Estimating summertime precipitation from Himawari-8 and global forecast system based on machine learning. *IEEE Trans. Geosci. Remote Sens.* **2018**, *57*, 2557–2570. [[CrossRef](#)]
27. Porcú, F.; Borga, M.; Prodi, F. Rainfall estimation by combining radar and infrared satellite data for nowcasting purposes. *Meteorol. Appl.* **1999**, *6*, 289–300. [[CrossRef](#)]
28. Yang, J.; Zhang, Z.; Wei, C.; Lu, F.; Guo, Q. Introducing the new generation of Chinese geostationary weather satellites, Fengyun-4. *Bull. Am. Meteorol. Soc.* **2017**, *98*, 1637–1658. [[CrossRef](#)]
29. Zhang, P.; Zhu, L.; Tang, S.; Gao, L.; Chen, L.; Zheng, W.; Han, X.; Chen, J.; Shao, J. General comparison of FY-4A / AGRI with other GEO/LEO instruments and its potential and challenges in non-meteorological applications. *Front. Earth Sci.* **2019**, *6*, 224. [[CrossRef](#)]
30. Zeng, X. The relationship among precipitation, cloud-top temperature, and precipitable water over the tropics. *J. Clim.* **1999**, *12*, 2503–2514. [[CrossRef](#)]
31. Tang, G.; Clark, M.P.; Papalexiou, S.M.; Ma, Z.; Hong, Y. Have satellite precipitation products improved over last two decades? A comprehensive comparison of GPM IMERG with nine satellite and reanalysis datasets. *Remote Sens. Environ.* **2020**, *240*, 111697. [[CrossRef](#)]
32. Foelsche, U.; Kirchengast, G.; Fuchsberger, J.; Tan, J.; Petersen, W.A. Evaluation of GPM IMERG Early, Late, and Final rainfall estimates using WegenerNet gauge data in southeastern Austria. *Hydrol. Earth Syst. Sci.* **2017**, *21*, 6559–6572. [[CrossRef](#)]
33. Li, X. Status of QPEs from Fengyun-4A satellites. In Proceedings of the 48th Meeting of The Coordination Group for Meteorological Satellites, Darmstadt, Germany, 25–29 May 2020 and 25–26 August 2020.
34. Ran, Y. FY-4A Precipitation Estimation Real-Time Product Format Description. Available online: http://img.nsmc.org.cn/PORTAL/NSMC/DATASERVICE/DataFormat/FY4A/Data/Format/FY4A_AGRI_L2_QPE_V1.1.pdf (accessed on 6 November 2022).
35. Liu, P.; Li, C.; Wang, Y.; Fu, Y. Climatic characteristics of convective and stratiform precipitation over the Tropical and Subtropical areas as derived from TRMM PR. *Sci. China Earth Sci.* **2013**, *56*, 375–385. [[CrossRef](#)]
36. “Rain”, Glossary of Meteorology, American Meteorological Society. Available online: <https://web.archive.org/web/20220131203129/https://glossary.ametsoc.org/wiki/Rain> (accessed on 22 October 2022).
37. Heinemann, T.; Kerényi, J. The EUMETSAT multi sensor precipitation estimate (MPE): Concept and validation. In Proceedings of the EUMETSAT Users Conference, Weimar, Germany, 29 September–3 October 2003.

38. Xiao, X.; Lian, S.; Luo, Z.; Li, S. Weighted Res-UNet for High-Quality Retina Vessel Segmentation. In Proceedings of the 2018 9th International Conference on Information Technology in Medicine and Education (ITME), Hangzhou, China, 19–21 October 2018; pp. 327–331.
39. Min, M.; Wu, C.; Li, C.; Liu, H.; Xu, N.; Wu, X.; Chen, L.; Wang, F.; Sun, F.; Qin, D. Developing the science product algorithm testbed for Chinese next-generation geostationary meteorological satellites: Fengyun-4 series. *J. Meteorol. Res.* **2017**, *31*, 708–719. [[CrossRef](#)]

Disclaimer/Publisher’s Note: The statements, opinions and data contained in all publications are solely those of the individual author(s) and contributor(s) and not of MDPI and/or the editor(s). MDPI and/or the editor(s) disclaim responsibility for any injury to people or property resulting from any ideas, methods, instructions or products referred to in the content.